ACS OMEGA

http://pubs.acs.org/journal/acsodf

Article

Study of the Fluidized Separation Process of Irregular Coarse-Grained Pulverized Coal Agglomerates Based on Modified Computational Fluid Dynamics—Population Balance Method

Jianxiang Zheng, Jiacheng Lu, Chenmin Ma, Tai Lv, and Hongbo Lu*

Cite This: *ACS Omega* 2022, 7, 21750−21762

Read Online

ACCESS | Metrics & More | Article Recommendations

ABSTRACT: In this work, the agglomeration, fragmentation, and separation process of coarse-grained pulverized coal agglomerates (CGPCA) obtained from a power plant were achieved using gas−solid fluidized bed sorting and analyzed through a combination of numerical simulations and actual experiments with CGPCA. To study the polydispersity and irregularity of CGPCA, the CGPCA surface fractal dimension was calculated using fractal dimension combined with scanning electron microscopy. The two-section fractal dimension of the particle size distribution was obtained by fitting the logarithmic particle size distribution of CGPCA. On the basis of the obtained data, the polydisperse particle drag force model, the agglomeration kernel function, and the breakage kernel function were modified. Thus, an irregular polydisperse gas−solid two-phase Eulerian−Eulerian model was constructed to simulate the sorting process of CGPCA in the fluidized bed. The results of the numerical simulation investigation were compared with the experimental results and showed that the simulation data, which considered the two section fractal dimension, was in better agreement with the experimental results. The cumulative logarithmic distribution of CGPCA's size was segmented and fitted. The values of the two section fractals of the agglomerates were determined as D = 1.014 and D = 2.401, respectively. Analysis revealed that the optimal separation efficiency working condition in the simulation process, providing the highest separation efficiency of 54.7%, was generated at air velocity of 1.21 m/s.

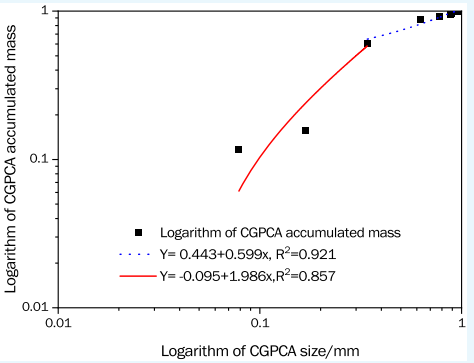

1. INTRODUCTION

Currently, more than 90% of coal-fired power plants in China use pulverized coal combustion methods, and the coal-grinding system is a necessary process. It is known that the energy consumption of the coal-grinding system is the largest among auxiliary equipment.[1] During the coal grinding process, coarse-grained pulverized coal agglomerates (CGPCA) are produced by the classifier inside the mill and are returned to the grinding disc for regrinding. CGPCA is rich in hazardous minerals, such as pyrite. Pyrite is a very dense mineral, mainly found in the form of microcrystalline particles embedded in CGPCA,[2] and its shape is irregular, difficult to grind, and a source of sulfur dioxide (SO_2). This mineral circulates in the mill many times, resulting in an increased mill cycle ratio (the ratio of the separator feed to the qualified coal powder). According to on-site investigations, the cycle ratio in power plants located in China can even reach 10−12 times. A high cycle rate reduces coal grinding efficiency and increases power consumption, while burning coal powder containing pyrite in the furnace causes problems such as SO_2 pollution and slagging in the furnace.[3] Therefore, the reduction of pyrite is considered a vital area of research.

To overcome the aforementioned issue, dry separation is an effective method for gas−solid fluidized separation.[4−8] The application of simulation methods to study this separation process must consider two aspects: the first is the size evolution process of CGPCA, and the second is the applicability of the drag model for irregular agglomerates.

In the case of the first aspect, during the separation process, particles agglomerate and break up due to the combined action of Brownian, van der Waals, electrostatic, hydrodynamic, and gravity forces, resulting in changes in the number and size of particles.[9,10] The milled coal particles undergo primary agglomeration due to intermolecular forces, and then secondary agglomeration and fragmentation form in the fluidization and sorting process.[11] Computational Fluid Dynamics (CFD)−Population Balance Method (PBM) is an economical and effective method to simulate the evolution process of the number and size of particles caused by agglomeration and fragmentation in the fluidization process.[12]

Received: March 25, 2022
Accepted: May 31, 2022
Published: June 15, 2022

https://doi.org/10.1021/acsomega.2c01825
ACS Omega 2022, 7, 21750−21762

In order to study the agglomeration and fragmentation behavior, researchers have investigated the fragmentation of droplets, bubbles, and solid particles alike. Additionally, based on the PBM model, its breakage kernel function was studied. However, the fragmentation of solid agglomerates is mainly related to the surface energy of the agglomerates,[13] particle collision, and unique characteristics that have a great impact on the fragmentation, such as the shape, structure, and size. Hence, when examining the fragmentation nucleus function, one should consider the influence of the irregularity of the particles on the fragmentation process. The irregularity of the agglomerates can be expressed in fractal dimensions. The particle size distribution of the particles follows the rosin-rammler function distribution and G-S distribution, both of which have been shown to have fractal characteristics. The relationship between agglomerate particle size and fractal dimension is self-similar and scale-invariant in properties. Therefore, the calculation of the kernel function should consider the calculation of the multiple fractal dimension for different particle sizes.[14,15]

In the case of the second aspect, most studies regard particles as perfect spherical particles[16] because the fluid flow in dense and polydisperse multiphase systems is very complicated. The particles are often different in size, shape, and material, in which the first two cause the drag force model to be nonuniversal,[16] which plays a vital role in the fluidization process simulation. Research and selection of a suitable drag force model has become an important issue in achieving gas−solid fluidization models.

For nonspherical drag force models, Neale et al.[17] derived an expression for the permeability sphere traction force under the condition of $Re < 0.1$ and proposed a theoretical formula for the factor ratio of the drag force. Johnson et al.[18] experimentally and theoretically analyzed the drag coefficient function of fractal agglomerates between 100 and 1000 μm at low Reynolds numbers, showing that the agglomerates can be viewed as a porous fractal structure in terms of structure. Tsou et al.[19] and Wu et al.[20,21] conducted flow experiments with high porosity spheres and concluded that the flow field in their wake did not change significantly because the fluid is able to pass through its internal pores. They extended the applicability of the Reynolds number in the Stokes equation by considering the fractal structure inside the flocculent agglomerates, where the fractal dimension was estimated by free settling tests or simulations. Tan et al. showed that the effect of the porous structure on the drag coefficient can be expressed in terms of fractal dimension. In our presented study, we construct a fractal drag model based on this method.

The two aforementioned aspects suggest that the morphology of particle agglomerates needs to be considered fractally. The particle agglomerate morphology is related to the fractal properties of particle size and shape. The dimensional fractal properties of the resulting fragmentation products have been characterized by Tyler et al. and Ahmed et al.,[22,23] where the fractal dimension is a representation of particle fragmentation and size distribution. Wang et al.[24] proposed a fractal segmental fitting theory to provide a multiscale interpretation of scale effects. In our presented study, we will derive the kernel equation for aggregated nucleus fragmentation related to CGPCA size distribution and the nonregular drag force model based on the multiscale fractal dimension.

Herein, a CFD-PBM model of irregular agglomerate fluidization was constructed for the CGPCA separation process. The research was divided into three parts: First, the fractal characteristics of CGPCA and calculation of related physical quantities were addressed. Second, considering the multiple fractal characteristics of the distribution of agglomerate particle size, the fractal drag force formula was introduced, and the kernel function formula was modified. Third, a comparison with the separation experimental process for verification was performed. The direct quadrature method of moments (DQMOM) was used to discretize PBM, and the modified model was imported into the CFD workbench using the User Define Function (UDF). The experimental process was simulated for comparative validation.

2. CALCULATION OF CGCPA FRACTAL CHARACTERISTICS AND RELATED PHYSICAL QUANTITIES

2.1. Size Distribution Fractal of CGPCA. In recent years, with the rapid development and wide application of ultrafine grinding technology, the multidomain degree characteristics of particle size fractal under ultrafine grinding conditions have become a topic of interest for many studies,[25,26] i.e., the multidomain degree fractal of particle size distribution, which mainly is a double-domain fractal. It can be expected that the multidomain fractal characteristics are closely related to the

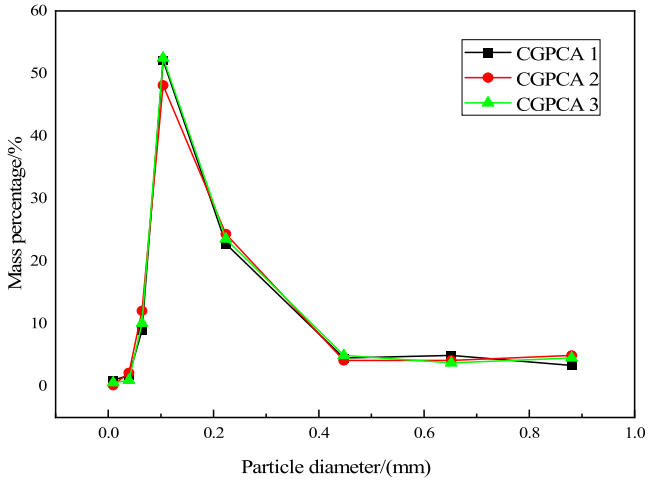

Figure 1. Particle size distribution of CGPCA.

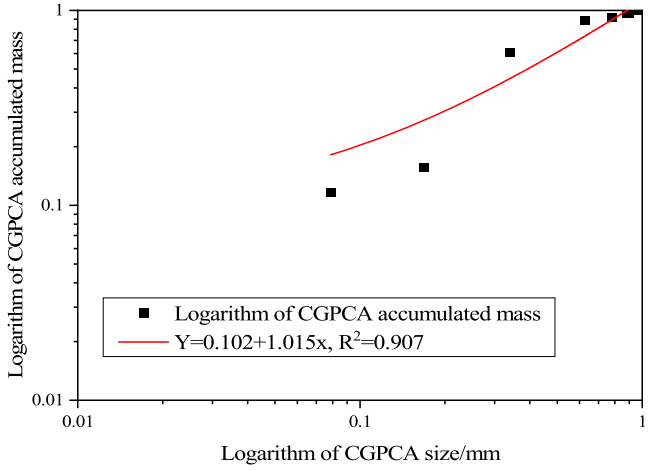

Figure 2. One-section fractal dimension fitting diagram based on the logarithmic distribution of CGPCA size.

https://doi.org/10.1021/acsomega.2c01825
ACS Omega 2022, 7, 21750−21762

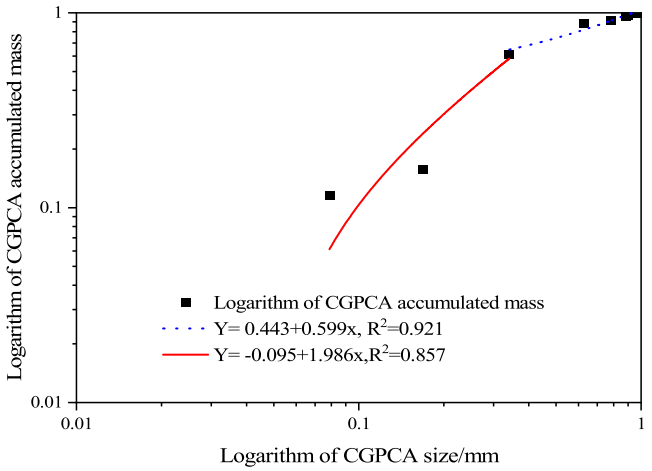

Figure 3. Two-section fractal fitting diagram based on the logarithmic distribution of particle size.

comminution force and method of the ultrafine grinding process. We confirmed this theory by studying the particle size distribution under different comminution environments.

The fractal dimension of the particle size distribution was calculated using eq 1.

$$\frac{M(<d)}{M_T} = \left(\frac{d}{d_{max}}\right)^{3-D} \quad (1)$$

where $M(<d)$ is the accumulated mass of the particle; M_T is the total mass of the sample; d is the particle size; d_{max} is the theoretical maximum size of the sample; and D is the fractal dimension of the particle size distribution. Equation 2 is obtained by simultaneous logarithmic changes on both sides of the above equation.

$$\log\left[\frac{M(<d)}{M_T}\right] = (3 - D)\log d + c \quad (2)$$

The slope of the fitted line, k, is obtained by fitting a straight line in a double logarithmic curve coordinate system using the least-squares method. By fitting the slope of the line, the fractal dimension of the particle size distribution D is found, and the relationship between k and the fractal dimension is as follows:

$$k = 3 - D \quad (3)$$

The surface fractal dimension D_s is related to the shape fractal D_p as follows:

$$D_s = D_p + 1 \quad (4)$$

Three samples of 500 g of CGPCA were procured from the powder return pipe of the coal pulverizer, and each sample was

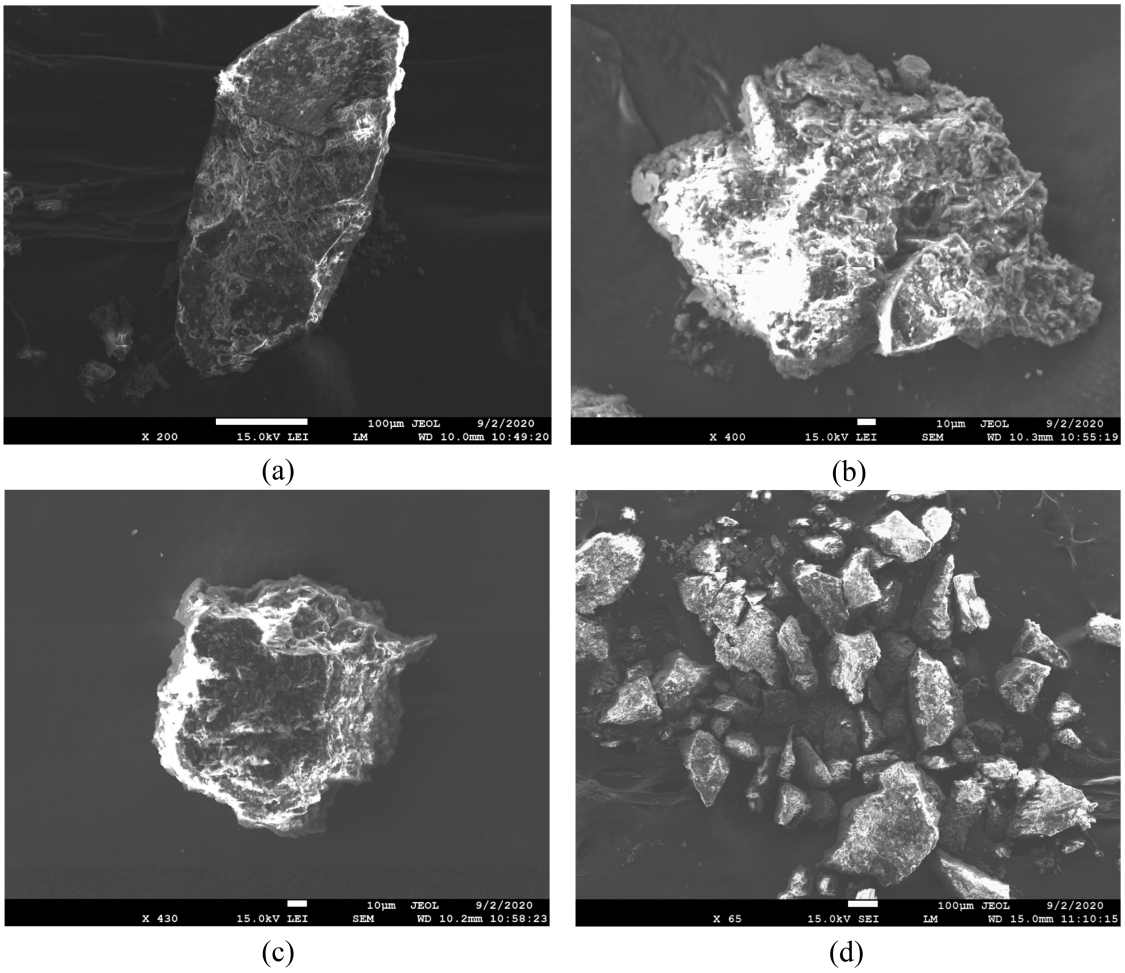

Figure 4. (a, b, and c) Electron microscope scan image of CGPCA of different shapes. (d) Electron microscope scan image of CGPCA size distribution. These images are copyrighted by the author.

https://doi.org/10.1021/acsomega.2c01825
ACS Omega 2022, 7, 21750−21762

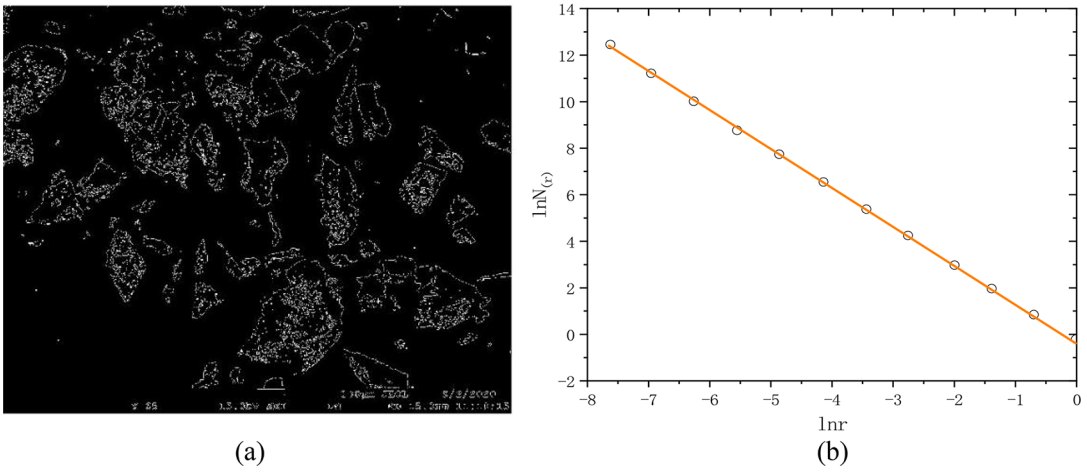

Figure 5. (a) Binary image of agglomerates. (b) $D_p = \ln N(r)/\ln(1/r)$.

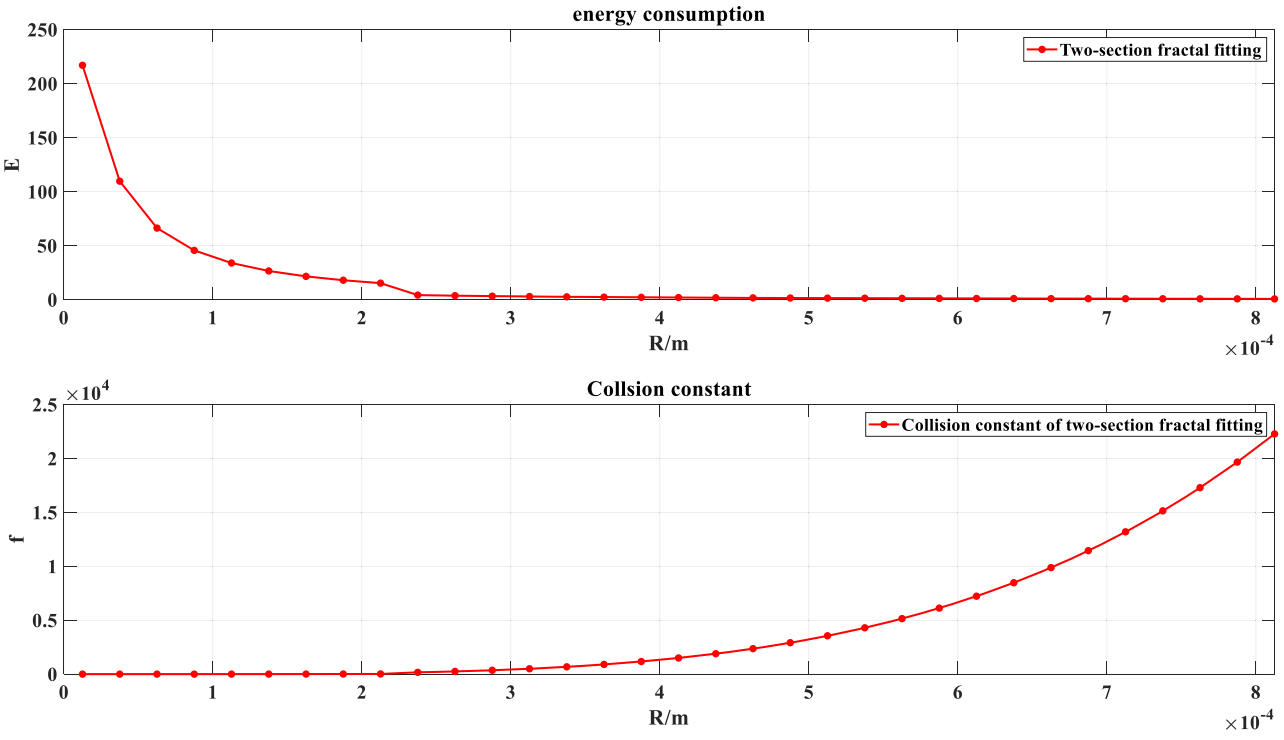

Figure 6. Collision constant and energy consumption of two-section fractal fitting.

recorded as CGPCA1, CGPCA2, and CGPCA3. Electronic vibrating sieves (model: S49-1000) were employed to sieve three samples. The particle size composition of CGPCA is shown in Figure 1.

As shown in Figure 1, the particle size range of CGPCA was 0.105−0.22 mm, 0.22−0.45 mm, and 0.063−0.105 mm, respectively. The average percentages were 51.36%, 22.42%, and 11.72%, respectively. These three percentages account for 85% of the total CGPCA quality. The part less than 0.063 mm was approximately 2%, and the particles larger than 0.45 mm account for approximately 12−13% of the total. Figure 1 shows that the particle size distribution of the obtained CGPCA was a typical partial normal distribution, which belonged to the wide-size distribution particles.

Figure 2 shows the one-section fractal fitting diagram based on the logarithmic distribution of CGPCA size. According to eq 2, the cumulative mass curve of the particle size distribution of CGPCA was fitted and calculated, and the slope of the fitted curve obtained was $k = 1.015$. Hence, the fractal dimension was calculated as $D = 1.985$ according to eq 3. The fitting variance was determined as 0.907, which satisfied the fitting accuracy requirement. This was regarded as the average fractal dimension of the whole particle size distribution range and used to calculate the average traction force. At the same time, in order to calculate the surface energy in the breakage process, considering the calculation accuracy and efficiency, the particle size in two sections was fitted and the fractal dimension of the particle size in two sections was obtained. The fitted curves are shown in Figure 3.

2.2. Fractal Characteristics of Surface Morphology of CGPCA. The surface fractal dimension was obtained by scanning electron microscope (SEM) and box dimension analysis. The details were as follows.

https://doi.org/10.1021/acsomega.2c01825
ACS Omega 2022, 7, 21750−21762

Figure 4 shows a scanning image from an electron microscope, where the shape and size of coal particles were determined as different. A single calculation of CGPCA as spherical particles led to statistical errors in calculating essential parameters, such as the drag coefficient.

Fractal theory is currently the most suitable theory to describe the morphology of agglomerates, mainly due to the particle agglomerate system being nonlinear, stochastic, and dissipative in the evolution process. The "box counting method" was employed to calculate the surface fractal dimension of CGPCA based on the images obtained by SEM. The calculation procedure was as follows:

1. Determination of whether the image was an $N \times N$ image.
2. If not an $N \times N$ size image, then the image was transformed into an $N \times N$ size image and divided into $s \times s$ sub-blocks, where $N/2 \geq s > 1$, and s is an integer.
3. The grayscale image was a three-dimensional grayscale image, where X,Y represents the image's position. The Z axis represents the gray value.

The X,Y plane was divided into $s \times s$ grids. Assuming that the minimum and maximum values in an (i,j) grid fall in k and l boxes, respectively, the number of boxes covering the (i,j) grid was n_r, where $n_r = l - k + 1$. Assuming that the total number of boxes covering the entire image was N_r, where $N_r = \Sigma n_r(i,j)$.

$$D_p = \lim \frac{\ln N_r}{\ln(1/r)} \tag{5}$$

Figure 5 shows the binary image calculated by combining the SEM image with MATLAB. The facial fractal dimension calculated by this process was $D_p = 1.66$. Combined with Figure 6, we analytically concluded that the rate constant of particle breakage increased with increasing turbulence and particle size. However, particles or flakes with low fractal size were easily fragmented due to their small surface contact energy. Additionally, according to the calculation of the fractal size, particles with small particle size were close to spherical shape and had a small fragmentation probability f, while particles with large particle sizes were more irregular and fragmented more easily after agglomeration. Therefore, large particles were more likely to undergo fragmentation.

3. MATHEMATICAL MODEL

In this work, the Euler–Euler two-fluid model was used to construct the gas–solid fluidized model of polydisperse agglomerates. The solid phase flow adopts the Kinetic Theory of Granular Flow (KTGF) model, and the specific boundary conditions and formula descriptions are in the literature.[27] Considering the effect of the nonspherical structure of agglomerates on the flow and agglomerate fragmentation process, we introduced the multiple fractal dimension to modify the drag force equation and PBM model. The modified drag force model and agglomerates collision and fragmentation models are detailed below.

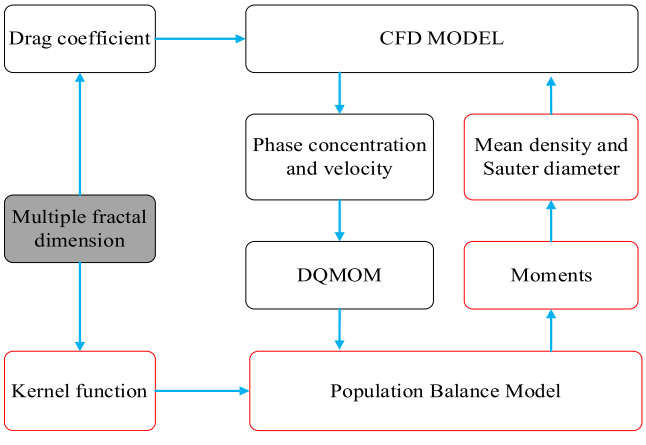

Figure 7. CFD–PBM coupling algorithm.

3.1. Equation of Interaction in Gas–Solid Phase. Drag formula:

$$F_D = \beta(v_g - v_s) \tag{6}$$

Drag coefficient:

$$\beta = \begin{cases} \frac{3}{4}\frac{\rho_g(1-\varepsilon_g)\varepsilon_g}{d_\rho}|v_g - v_s|\varepsilon_g^{-2.7}C_d & \varepsilon_g > 0.8 \\ 150\frac{(1-\varepsilon_g)^2\mu_g}{\Omega^2\varepsilon_g {d_\rho}^2} + 1.75\frac{(1-\varepsilon_g)\rho_g|v_g - v_s|}{\Omega d_\rho} & \varepsilon_g \leq 0.8 \end{cases} \tag{7}$$

Reports have shown that the drag coefficient is related to the internal porosity of the particle aggregates, which has fractal characteristics. Therefore, the drag force of particle agglomerates can be modeled with different fractal dimensions and Reynolds numbers.[28]

When $Re = 40–400$, the formula is

$$C_d = Re^{-0.7}(-447.42 + 314.8D - 52.56D^2) \quad Re = 0.1 - 20 \tag{8}$$

$$C_d = 0.66Re^{-0.63}D^{3.97} \quad Re = 20 - 40 \tag{9}$$

$$C_d = 1.85D^{13.058}Re^{-0.32}/10^5 \quad Re = 40 - 400 \tag{10}$$

C_d is drag coefficient, Re is the Renold number, and D is the fractal dimension.

3.2. Population Balance Model. The PBM was used to describe the microscopic evolution of agglomerates size during the gas–solid separation process. It is known that the population balance equation is a continuous equation regarding the agglomerates' density function. The constitutive equation is as follows:

$$\frac{\partial}{\partial t}[n(V,t)] + \nabla\cdot[\vec{u}n(V,t)] = \underbrace{\frac{1}{2}\int_0^V \beta(V-V',V')n(V-V',t)n(V',t)\,dV'}_{\text{Birth due to Aggregation}} - \underbrace{\int_0^\infty \beta(V,V')n(V-V',t)n(V',t)\,dV'}_{\text{Death due to Aggregation}} + \underbrace{\int_{\Omega_V} \rho f(V|V')n(V',t)\,dV'}_{\text{Birth due to Breakage}} - \underbrace{f(V)n(V,t)}_{\text{Death due to Breakage}} \tag{11}$$

During gas–solid separation, the size evolution of agglomerates was due to aggregation and breakage of particles under the action of forces leading to the generation and death of particle agglomerates. These forces originate from Brownian motion, turbulent motion, and gravitational effects.[29]

https://doi.org/10.1021/acsomega.2c01825
ACS Omega 2022, 7, 21750–21762

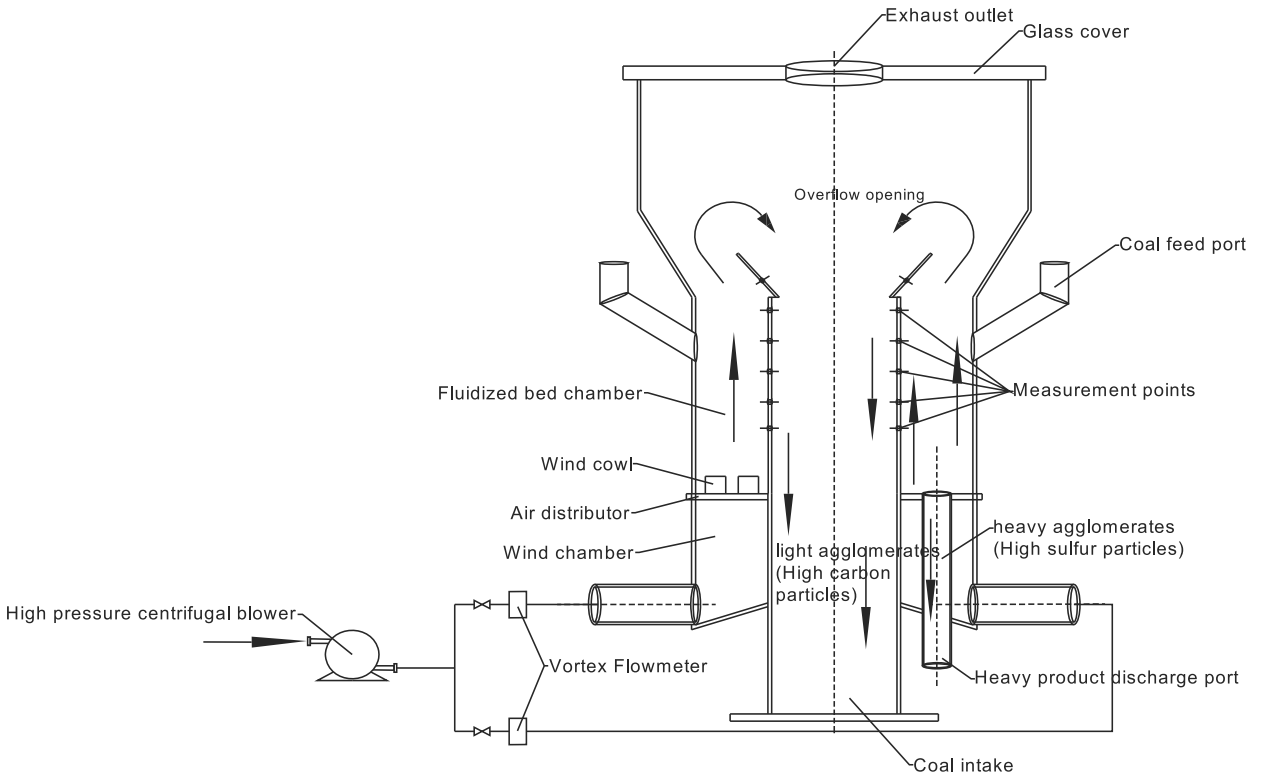

Figure 8. A schematic diagram of the experimental platform.

Ramkrishna and Singh[30] analyzed agglomerates and breakage kernel functions under different stressing mechanisms. The analysis shows that the variation of agglomerate kernel function was influenced by different external force conditions and the particle's internal conditions (size, shape), which leads to the kernel function formulas for Brownian agglomerates, turbulent agglomerate kernels, and differential settling agglomerates. Furthermore, the nonspherical structure and porous shape of particle agglomerates affected agglomerate collisions. Hence, the fractal structure and porous permeability should be introduced to represent the effect of particle structure on collisions. Somasundaran and Runkana[31] suggested that the function to calculate the collision frequency must consider both the permeability and fractal dimension of the agglomerates. Zheng et al.[32] analyzed and compared the agglomeration kernel function in the fractal dimension and obtained the root-mean-square model. In our work, the model was applied to analyze the agglomeration process. The specific mathematical model is shown in ref 32.

3.3. Breakage Model. Song et sl.[33] summarized several breakage models, including the uniform failure model, parabolic model, and empirical failure model. The study focused on the mechanism of the droplet or bubble breakage. In the case of CGPCA originating from ball tube mills fluidized and sorted in a fluidized bed, agglomeration fragmentation is mainly influenced by the flow field, particle-wall collisions, and particle−particle collisions. Hence, this report employed the Ghadiri solid particle breaking model—the parabolic model,[34] On the basis of the principle of particle collision energy conservation, the following collision frequency formula was obtained.

$$f = \frac{\rho_s E^{2/3}}{\Gamma^{5/3}} v^2 L^{5/3} = K_b v^2 L^{5/3} \tag{12}$$

ρ_s is the particle density, E is the elastic modulus of the particle, Γ is the interface energy, V is the impact velocity, L is the preferred particle diameter, and K_b is the damage constant defined as

$$K_b = \frac{\rho_s E^2/3}{\Gamma^{5/3}} \tag{13}$$

Typical interface energy formulas were summarized in previous reports, but they did not correlate surface energy with particle shape and surface roughness. Therefore, the energy required for agglomerate fragmentation was related to the surface energy, and the surface energy magnitude was related to the size and shape of the particles. Carpinteri and Pugno[35] suggested that agglomerates have self-similarity and scale-invariance.

However, fractals in nature do not have standard self-similarity but rather self-similarity in a statistical sense. That is, its self-similarity exists within a certain scale range, and the two ends are often limited by some characteristic scale. This range is called the scale-free area, where the fractal system has scale-invariance.

After fragmentation, the surface energy can be corrected by introducing fractal dimension. On the basis of the DOVL theory, Wang et al.[24] fitted the surface energy equation for the multiple fractal dimensions of coal powder:

$$E = \frac{(3 - D_1)C}{(3 - D_s)x_2^{3-D_1}}\left(\frac{x_2^{D_s-D_1}}{D_s - D_1} - \frac{x_1^{D_s-D_1}}{D_s - D_1}\right) + \frac{(3 - D_2)C}{(3 - D_s)x_2^{3-D_2}}\left(\frac{x_2^{D_s-D_2}}{D_s - D_2} - \frac{x_1^{D_s-D_2}}{D_s - D_2}\right) \tag{14}$$

According to the results of the log−linear fit in Figure 2, the fractal dimension D = 1.014 for the particle size range <0.22 mm, and D = 2.401 for the particle size range >0.22 mm. As the

https://doi.org/10.1021/acsomega.2c01825
ACS Omega 2022, 7, 21750−21762

(A) External view of the experiment bench

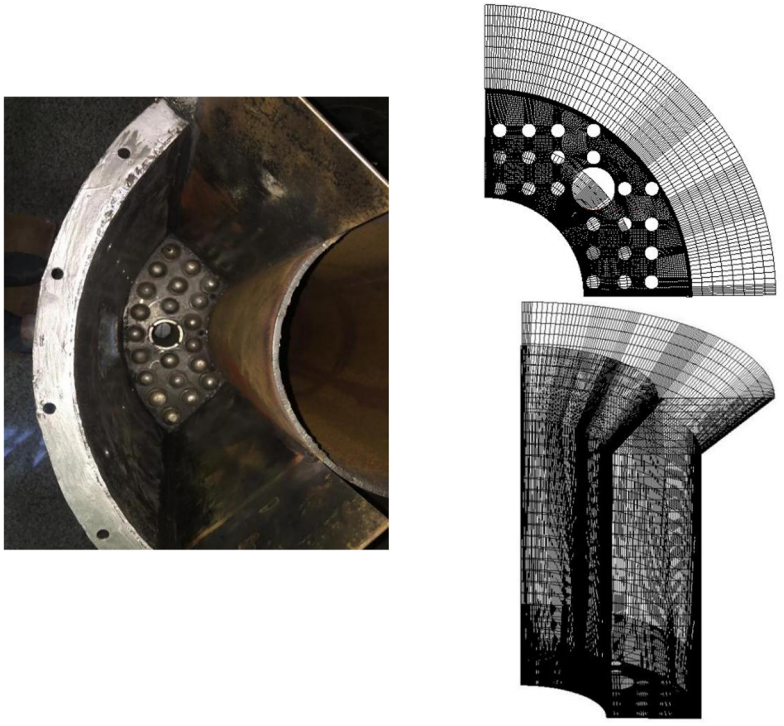

（B）Internal diagram of the experiment bench

Figure 9. (A, B) The internal and external views of the experiment bench and the simulation grid diagram.

particle size decreases, the crushing mode of particles changes from separation between particles to the expansion of cracks, and then it develops into crushing. The shear slip is inside the particles until the fracture of the mineral lattice. In this process, the fractal dimension of the particle size gradually decreases and the energy consumption gradually increases. Fractal dimension can also show the change of energy consumption in the process of particle crushing, where the smaller the fractal dimension, the greater the energy consumption, and the more difficult the particles are to crush. Therefore, as shown in Figure 6, the fractal dimension used for the calculation of crushing energy was different in different particle sizes. In order to accurately calculate the size of E, eqs 14 and 4 were used—the surface dimension.

The two-way couple of CFD-PBM is shown in Figure 7. First, the parameters related to particle agglomeration, such as volume concentration and particle velocity of the particle phase, were obtained by solving the control equations in the gas−solid two-phase flow model. Second, PBM was solved using these parameters to obtain the moment information. Then, the information was used to obtain the Sauter diameter of the particle phase, which was further corrected for the interphase forces in the gas−solid two-phase flow model. Finally, the volume fraction and velocity of the particle phase were updated by correcting the interphase forces. After such a closed cycle, a complete iterative process was achieved. In the calculation process, UDF was applied to allow the multifractal dimension

https://doi.org/10.1021/acsomega.2c01825
ACS Omega 2022, 7, 21750−21762

into the kernel model and traction coefficient. The correction of the model was completed.

4. PHYSICAL MODEL AND RELATED PARAMETER CALCULATION

Figure 8 shows a schematic diagram of the fluidized sieving experiment, which consists of an annular fluidized bed body, air supply control system, screw powder feeder, measuring instrument, and data acquisition system. The experimental process was as follows: The compressed air from the high-pressure centrifugal fan was sent into the isobaric air chamber of the annular fluidized bed through the vortex flowmeter. CGPCA was sent from the fluidized screw feeder, which was fluidized and separated by the air sent from chamber. The high-sulfur mineral content (called heavy agglomerates) was separated from CGPCA. The exhaust gas generated in the experiment was discharged through the exhaust outlet. The high-density minerals (heavy agglomerates) were discharged from the slag pipe, and the high-carbon particles (called light agglomerates) were separated into the annular inner cylinder.

Figure 9 shows the physical picture of the experimental bench and the grid diagram of the simplified quarter-circle gas–solid fluidized bed drawn using ANSYS ICEM. The proposed model was an annular gas–solid fluidized bed with a height of 0.55 m and a diameter of 0.28 m. Twenty-two velocity inlets with a diameter of 0.0186 m were opened at the bottom. At the beginning, the nonspherical agglomerates were piled at the bottom of the bed with an accumulation height of 0.08 m and an initial density of 700 kg/m^3. Fluidization was performed at room temperature with an air density of 1.225 kg/m^3 and viscosity of 1.8×10^5 Pa s. The gas entered through the inlet and exited through the top outlet, and the outlet was set as a micropositive pressure outlet. Simulations of comparative conditions under spherical, single fractal, and multiple fractal conditions were performed. The inlet velocity ranged from 0.2 to 1.2 m/s. DQMOM was chosen in the Population Balance Model and used for the calculation. The data of particle size distribution in the experiments were used to set the minimum to maximum size from 4×10^{-5} m to 8.8×10^{-4} m. The UDF method was applied to incorporate the multiple fractal dimension kernel function into the PBM model.

Table 1. Calculation Results of GCI

number of nodes	r	$f(C_{max})$	ε	GCI/%
380924	1.073	0.14935	0.0033	2.8
470584	1.051	0.14985	0.0028	2.89
546318	1.053	0.15027	0.0014	1.63
637868	—	0.15048	—	—

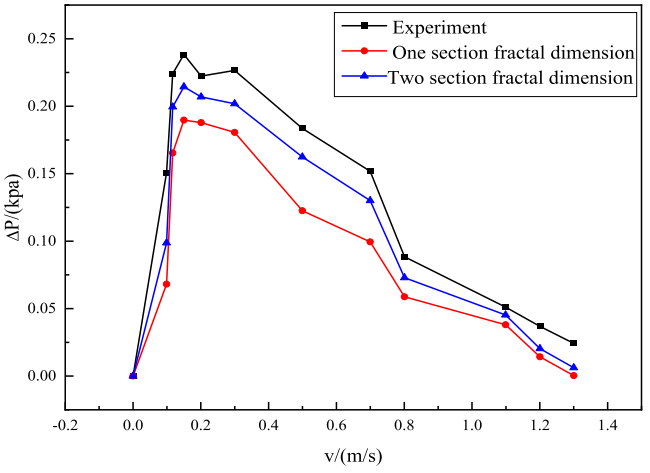

Figure 10. Pressure drop variation in the air velocity range of 0–1.3 m/s.

To select the appropriate number of meshes, mesh independence verification was performed. The number of nodes for mesh encryption is shown in Table 1. Increasing the number of meshes affected the time cost of the simulation; hence, the grid convergence index was used to evaluate the appropriate number of meshes.

According to the literature,[36,37] the mesh convergence error is expressed as eq 15:

$$\varepsilon = \frac{f_1 - f_2}{f_1} \tag{15}$$

where f_1 and f_2 are the convergent solutions for the fine and coarse meshes, respectively; f is the maximum concentration of light agglomerates taken.

The mesh encryption ratio is defined by eq 16:

$$r_{k,k+1} = \frac{h_k}{h_{k+1}} \tag{16}$$

where h_k is the average of spacing per mesh, calculated using eq 17:

$$h_k = \sqrt[3]{\frac{\sum_{i-1}^{N_k} \Delta V_i}{N_k}} \tag{17}$$

where ΔV_i is the volume of each mesh cell and N_k is the total number of nodes for each set of meshes

Furthermore, the mesh convergence index GCI was defined as eq 18:

$$\mathrm{GCI} = F_s \frac{|\varepsilon|}{r^p - 1} \tag{18}$$

where F_s is the safety factor. F_s = 3 when two grids are used to estimate GCI; F_s = 1.25 when three or more grids are used to estimate GCI. P is the convergence accuracy, taken as P = 1.97.

Calculation results of GCI are listed in Table 1.

The calculated results of GCI were 380 924, 470 584, and 546 318 for three sets of meshes, including 2.8%, 2.9%, and 1.63%, respectively, which were below 3% and satisfied the convergence index criterion.[38] After comprehensive evaluation, the numerical simulation values were independent of the number of meshes after the number of meshes was greater than 546 318.

Figure 10 shows the variation of pressure with fluidization air velocity obtained after the fluidization experiment for CGPCA from the coal crusher return pipe of the Jilin Chemical Fiber Plant. As shown in Figure 10, the pressure gradually increased as the fluidization air velocity increased, followed by the pressure of the CGPCA remaining essentially constant when CGPCA reached the fluidized state. Thus, the minimum fluidization velocity u_{mf} = 0.12 m/s was determined. The corresponding pressure drop ΔP = 0.22 kpa, and the flow velocity u in the bubbling bed stage was 0.12–0.5 m/s. The turbulent bed stage was $0.5 \leq u_{t1} \leq 0.72$ m/s, and the fast bed stage was $u_{t2} \geq 0.72$ m/s.

https://doi.org/10.1021/acsomega.2c01825
ACS Omega 2022, 7, 21750–21762

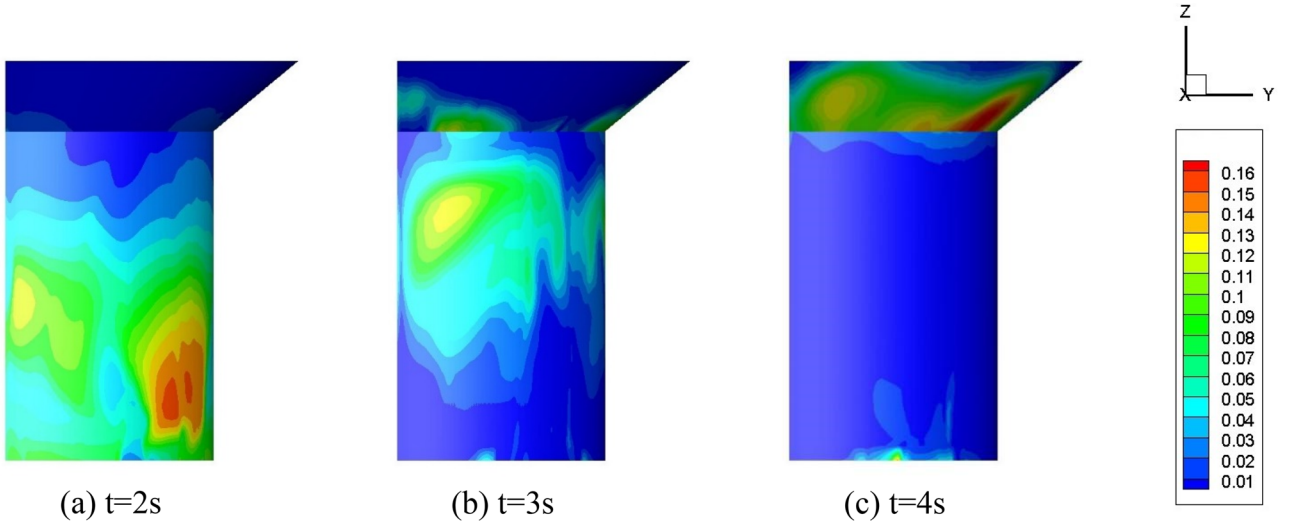

Figure 11. Instantaneous concentration distribution of light aggregates at (a) t = 2 s, (b) t = 3 s, and (c) t = 4 s at 1.1 m/s.

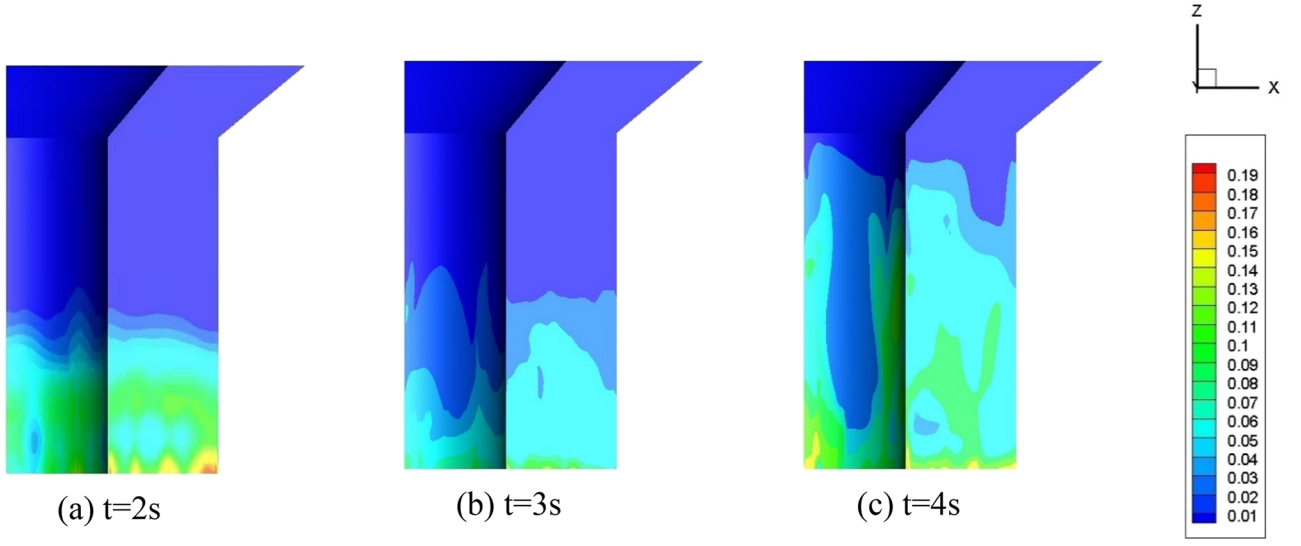

Figure 12. Instantaneous concentration distribution of heavy agglomerates at (a) t = 2 s, (b) t = 3 s, and (c) t = 4 s at 1.1 m/s.

Figure 10 compares the simulation results of one section fractal dimension D = 1.985, the simulation results for the two section fractal dimension, and experimental data. The obtained results were comparable to the experimental data results when considering the multiple fractal dimension. Therefore, the simulation results were more accurate when the fractal dimension was considered.

5. ANALYSIS OF BED VOLUME CONCENTRATION DISTRIBUTION AND SORTING EFFICIENCY

Figure 11 shows the transient distribution of light agglomerate concentration at an average velocity of 1.1 m/s at the inlet, with an initial bed stacking height of 80 cm, and a stacking mass of 3 kg. Figure 12 shows the transient distribution of heavy agglomerates under the same conditions. According to data presented in Figures 11 and 12, air was fed from the air distribution plate at the bottom. CGPCA started to fluidize through the air over time, and the expansion height of the light agglomerates was higher due to their low density; hence, they were easy to fluidize. The light agglomerates was discharged from the outlet after 4 s. The heavy agglomerates were constantly fluidized in the bed. Therefore, the light agglomerates with low sulfur content were separated using the appropriate fluidization air velocity.

Figure 13 shows the agglomeration temperature distribution of agglomerates using different one-section fractals, two-section fractals, and without considering fractal conditions. The agglomeration temperature indicated the intensity of agglomerate collisional pulsations.[39] The red color indicated the region of higher agglomerate temperature, which meant that the agglomerates collided more violently in this location and were prone to agglomeration and fragmentation. The agglomerate structure had great influence on the collisions. The results of the two-section fractal calculation showed that the collision impulse energy becomes stronger. Hence, considering the fractal actually considered the effect of the agglomerate shape on the anisotropic characteristics of the pulsation velocity. This promoted enhanced collision probability of the agglomerates, indicating that it is more likely for agglomeration and fragmentation occur.

Figure 14 shows the particle size distribution of the light and heavy agglomerates after separation, where the overall particle

https://doi.org/10.1021/acsomega.2c01825
ACS Omega 2022, 7, 21750−21762

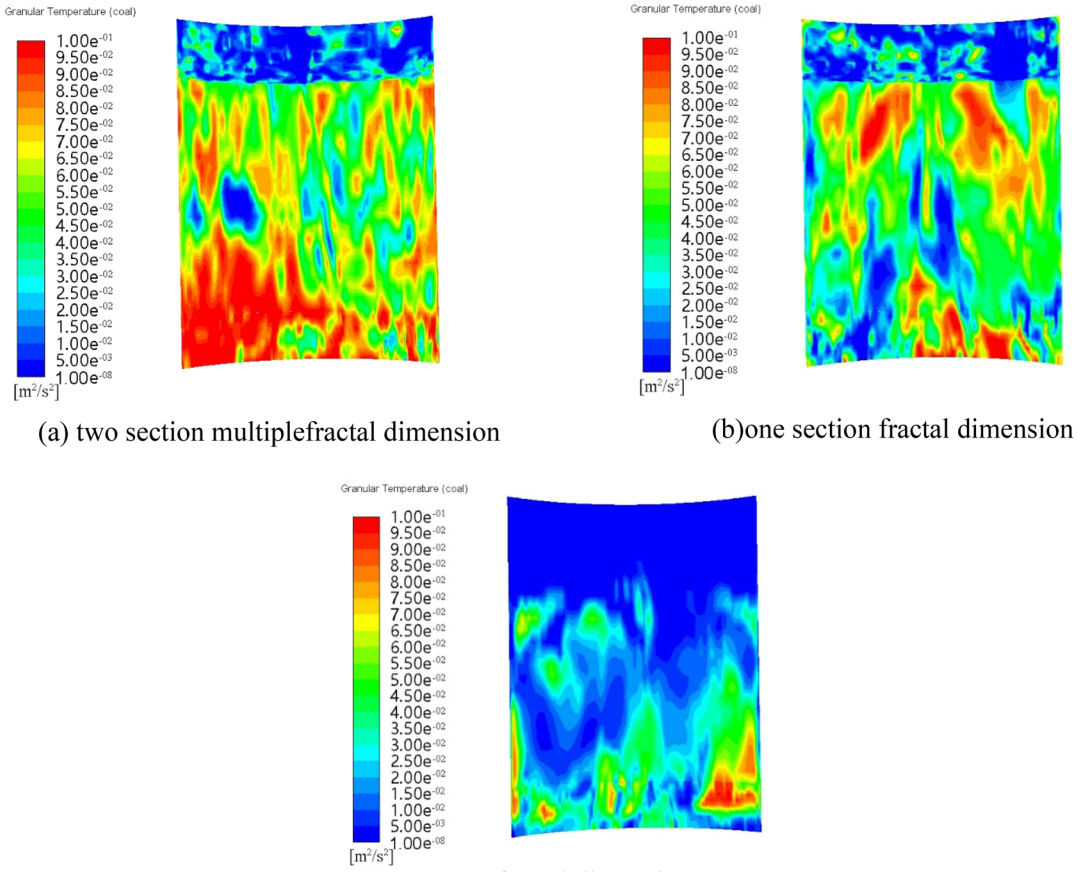

Figure 13. (a, b, c) Distribution of the average granular temperature of agglomerates with different fractal dimensions.

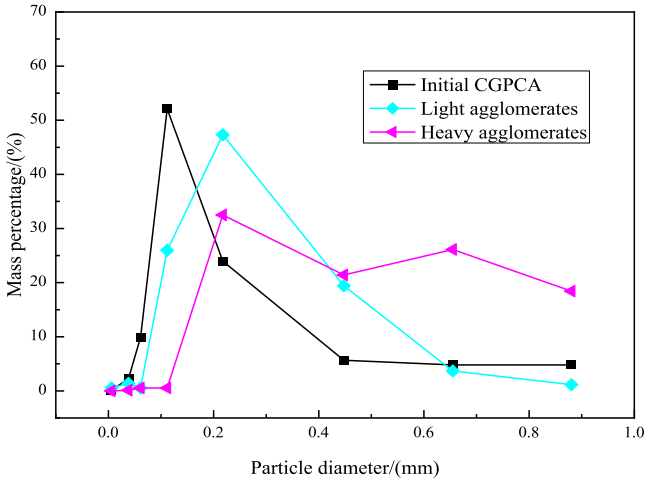

Figure 14. Average size distribution of the separation products (high-density minerals (heavy agglomerates) discharged from the slag pipe; high-carbon particles (light agglomerates) separated into the annular inner cylinder).

agglomerate average size increased after fluidization separation. This was corroborated by the variation of particle number over time (Figure 15). The heavier agglomerates had a larger average particle size and settled easily, allowing for effective separation. This reduced sulfur content of the light agglomerates.

During the CGPCA separation process, the total agglomerates number varied with time (Figure 15). Due to the significant difference between the densities of light and heavy agglomerates, the buoyancy force on light agglomerates was greater than the effect of gravity. Light agglomerates float up, and heavy agglomerates were discharged from the lower outlet. As time increased, the number of CGPCA (m_0) decreased gradually, and the agglomeration and then fragmentation occurred in the process, resulting in the number of particles (agglomerates m_0) being decreased first and then increased. Finally, the balance of quantity was reached, and the whole separation process was completed.

Figure 16 shows the separation efficiency of the process at different air velocities. Under this experimental condition, the separation effect was greater in the fast fluidized bed stage (air velocity > 1.10 m/s), where the Reynolds number in the process was above 500. Equation 19 determined the sulfur reduction efficiency.

$$\text{separation efficiency} = \frac{S_y - S_q}{S_y} \times 100\% \tag{19}$$

and eq 20 was employed to calculate the terminal velocity in this work.

$$u_t = \sqrt{\frac{4}{3}\frac{d_a(\rho_a - \rho_f)g}{0.43\rho_f}} \quad 500 < Re_t \tag{20}$$

S_y is the mass of pyrite of the light agglomerates in the coaltake. S_q is the mass of all pyrite in the CGPCA. A total of 3 kg of CGPCA was taken as the sorting sample. The sorting experiment was carried out in a rapid fluidization process. The masses of light agglomerates M_q and heavy agglomerates M_z

https://doi.org/10.1021/acsomega.2c01825
ACS Omega 2022, 7, 21750−21762

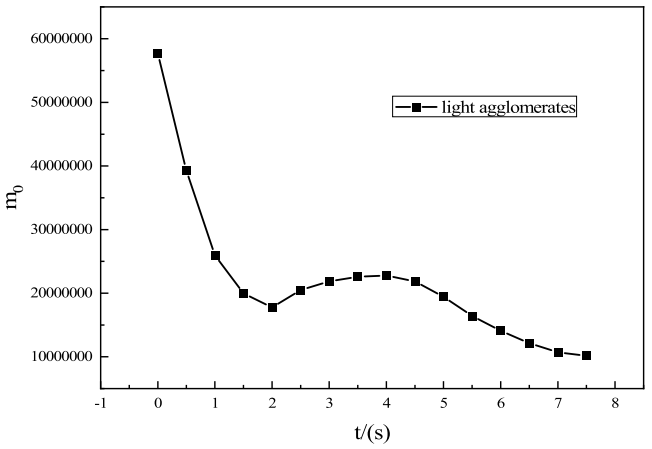

(a) light agglomerates m_0 change with time

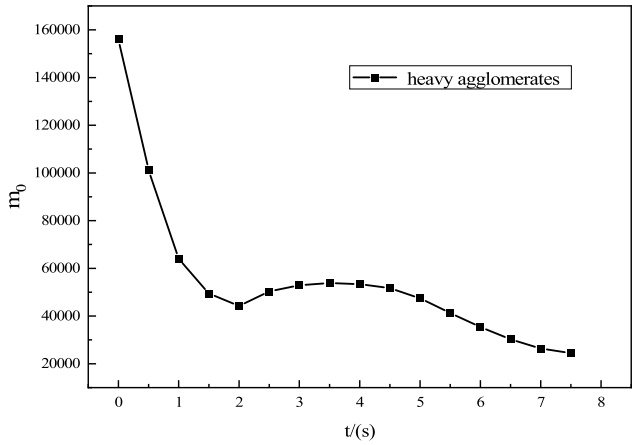

(b) heavy agglomerates m_0 change with time

Figure 15. (a, b) Different m_0 using DQMOM changes with time.

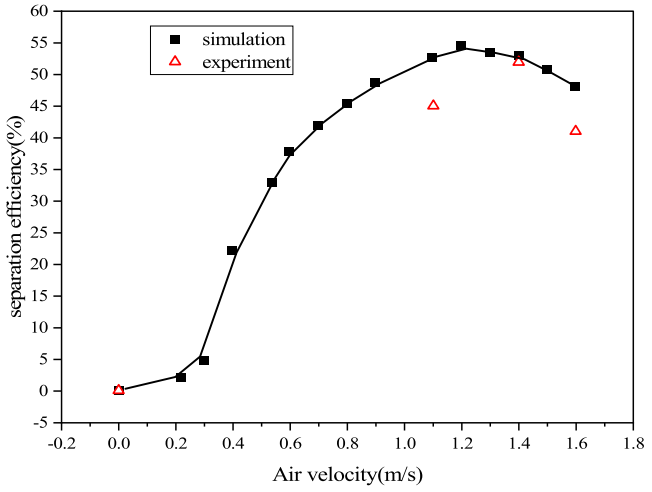

Figure 16. Separation efficiency at different air velocities.

were obtained by monitoring the coaltake and the discharge port, respectively. The samples, heavy aggregates, and light aggregates were also measured by fluorescence spectrometer (Model: EDX8600H). The amounts of pyrite were obtained as shown in Table 2. The mass of heavy agglomerates accounted for 9.24% of the mass of the sample. And the percentage of light agglomerates mass was 90.76%. Among them, the content of pyrite with an agglomerates size of less than 0.22 mm in the heavy agglomerates reached 6.34%. It indicated that the enrichment of pyrite occurred to the heavy agglomerates. Also, we performed three experiments at different air velocities, and the separation efficiency obtained is shown in Figure 16.

The average density was calculated according to the calculation method of dust-containing airflow density by Guo and Guo,[40] and the terminal entrainment velocity calculated by applying eq 20 was 1.212 m/s.

On the basis of the calculated results at the terminal velocity, the presented work analyzed the results of simulations performed at an air velocity of 1.21 m/s and calculated the separation efficiency of particle sieving at an air velocity of 54.7% using eq 20, where the results exceeded the separation efficiency of 52.89% observed experimentally at an air velocity of 1.393 m/s.

The obtained results were due to two reasons:

1. The results measured by the comparison experiment were not a continuous result, in which the measurement had a jump; hence, the obtained trend results were not completely accurate.

2. The air velocity of 1.393 m/s in the comparison experiment exceeded the critical entrainment air velocity obtained due to the calculation, which led to part of the heavy agglomerates being entrained and separated, resulting in lower separation efficiency.

6. CONCLUSION

In this work, numerical simulation combined with experimental research is used to study the separation and fluidization process of CGPCA. The main research conclusions were as follows:

A modified CFD−PBM model for gas−solid fluidization of nonspherical constructed polydisperse agglomerates was constructed. In the model, the multiple-fractal properties of agglomerate size were introduced to modify the drag coefficient model and breakage kernel model.

The cumulative logarithmic distribution of the agglomerate size of CGPCA was fitted in two sections. When the agglomerates size was less than 0.22 mm, the agglomerate fractal was $D = 1.014$, whereas when it was larger than 0.22 mm, the agglomerate fractal was $D = 2.401$.

The simulation results showed that, in the fluidization process, the particles were prone to agglomeration under turbulence in the early stage of fluidization, and some large particles could be broken down after the particle agglomeration had stabilized in the middle and late stages.

The simulation results based on the modified model were consistent with the experimental results, and obtained data combined with the simulation and experimental results showed that the final average separation efficiency was 54.7%.

Table 2. Amount of Pyrite in Each Separated Sample of the Experimental Sample (%)

	CGPCA	light agglomerates	heavy agglomerates	heavy agglomerates (<0.22 mm)	proportion of agglomerates	separation efficiency
amount of pyrite	2.78	1.44	4.68	6.34	9.24	52.89

https://doi.org/10.1021/acsomega.2c01825
ACS Omega 2022, 7, 21750−21762

AUTHOR INFORMATION

Corresponding Author

Hongbo Lu − *School of Energy and Power Engineering, Northeast Electric Power University, Jilin 132013, China*; Email: 552459916@qq.com

Authors

Jianxiang Zheng − *School of Energy and Power Engineering, Northeast Electric Power University, Jilin 132013, China*; orcid.org/0000-0002-8869-5606

Jiacheng Lu − *School of Energy and Power Engineering, Northeast Electric Power University, Jilin 132013, China*

Chenmin Ma − *School of Energy and Power Engineering, Northeast Electric Power University, Jilin 132013, China*

Tai Lv − *School of Energy and Power Engineering, Northeast Electric Power University, Jilin 132013, China*

Complete contact information is available at: https://pubs.acs.org/10.1021/acsomega.2c01825

Notes

The authors declare no competing financial interest.

ACKNOWLEDGMENTS

This work was supported by Jilin Provincial Science and Technology Department 13 Five-Year Plan Key Science and Technology R&D Projects (20180201001SF)

NOTATION

Re = the Reynolds number, −
C_d = drag coefficient, −
m_0 = number of the agglomerates, −
ρ_p = density of the agglomerates, kg/m^3
ρ_s = agglomerates density, kg/m^3
Γ = interface energy, J
v = impact velocity, m/s
L = preferred agglomerates diameter, m
K_b = damage constant, −
k_B = Boltzmann constant, J/K
T = absolute temperature, K
V, V' = actual volume of the particle agglomeration, m^3
P = agglomerates density, kg/m^3
D_1 = multiple fractal dimension in the large size, −
D_2 = multiple fractal dimension in the small size, −
C = mechanical crushing performance coefficient, −
D_p = surfacial fractal dimension, −
M = Aerodynamic viscosity, Pa·s
ε_d = turbulence dissipation rate per unit mass of fluid, m^2/s^3
$C_{D_i}C_{D_j}$ = cohesive agglomerates coefficient, −
u_{mf} = fluidization velocity, m/s
Δp = pressure drop, kpa
u_m = flow velocity, m/s
n_r = number of boxes in the grid, −
N_r = total number of boxes, −
S_y = sulfur content in raw coal, −
S_q = sulfur content in high-carbon agglomerates, −

REFERENCES

(1) Chen, B.; Ye, X.; Shen, J.; Wang, S.; Deng, S.; Yang, J. Investigations on the energy efficiency limits for industrial boiler operation and technical requirements—taking China's Hunan province as an example. *J. Energy*. **2021**, *220*, 119672.

(2) Wang, W.; Sang, S.; Bian, Z.; Duan, P.; Qian, F.; Lei, S.; Qin, Y. Fine-grained pyrite in some chinese coals. *J. Energy Exploration & Exploitation*. **2016**, *34* (4), 543−560.

(3) Xu, X. B.; Wu, J.; Wu, H. W.; Leng, J.; Liang, M.; Sheng, Z. Reforming the coarse powder separator to improve the economy of the boiler unit. *J. China Electric Power* **1999**, *07* (18), 19−75.

(4) Dong, L.; Zhou, E.; Cai, L.; Duan, C.; Zhao, Y.; Luo, Z. Fluidization characteristics of a pulsing dense-phase gas-solid fluidized bed for high-density separation of fine anthracite. *J. Energy & Fuels*. **2016**, *30* (9), 7180−7186.

(5) Fu, Y.; Chen, W.; Su, D.; Lv, B.; Luo, Z. Spatial characteristics of fluidization and separation in a gas-solid dense-phase fluidized bed. *J. Powder Technology*. **2020**, *362*, 246−256.

(6) Yan, S. N.; Wang, T. Y.; Tang, T. Q.; Ren, A. X.; He, Y. R. Simulation on hydrodynamics of non-spherical particulate system using a drag coefficient correlation based on artificial neural network. *J. Petroleum Science*. **2020**, *17* (2), 537−555.

(7) Zhang, X.; Han, Y.; Li, D.; Zhang, Z.; Ma, X. Study on attrition of spherical-shaped Mo/HZSM-5 catalyst for methane dehydro-aromatization in a gas-solid fluidized bed. *J. Chinese Journal of Chemical Engineering*. **2021**, *38*, 172−183.

(8) Lv, B.; Luo, Z.; Fu, Y.; Zhang, B.; Qin, X.; Zhu, X. Particle mixing behavior of fine coal in density control of gas-solid separation fluidized bed. *J. Particuology*. **2020**, *50*, 76−87.

(9) Frungieri, G.; Boccardo, G.; Buffo, A.; Marchisio, D.; Karimi-Varzaneh, H. A.; Vanni, M. A CFD-DEM approach to study the breakup of fractal agglomerates in an internal mixer. *J. The Canadian Journal of Chemical Engineering*. **2020**, *98* (9), 1880−1892.

(10) Zheng, J. X.; Wang, Z. Q. Numerical Simulation of the Acoustic Agglomeration Process of Coal-fired Fine Particles. *Journal of Northeast Electric Power University* **2019**, *39* (05), 65−71.

(11) Dosta, M.; Antonyuk, S.; Heinrich, S. Multiscale simulation of agglomerate breakage in fluidized beds. *J. Industrial & Engineering Chemistry Research*. **2013**, *52* (33), 11275−11281.

(12) Zheng, J.; Li, Y.; Wan, Z.; Hong, W.; Wang, L. Modification of the agglomeration kernel and simulation of the flow pattern in acoustic field with fine particles. *J. Powder Technology*. **2019**, *356*, 930−940.

(13) Kafui, D. Computer simulated impact of agglomerates. *J. Powders Grains* **1993**, 401−406.

(14) Perfect, E.; Kay, B. D. Applications of fractals in soil and tillage research: a review. *J. Soil and Tillage Research*. **1995**, *36* (1−2), 1−20.

(15) Li, X.; Su, W. The distributional dimension of fractals. *J. Analysis in Theory and Applications*. **2007**, *23* (3), 283−300.

(16) Nikku, M.; Jalali, P.; Ritvanen, J.; Hyppänen, T. Characterization method of average gas-solid drag for regular and irregular particle groups. *J. Powder technology*. **2014**, *253*, 284−294.

(17) Neale, G.; Epstein, N.; Nader, W. Creeping flow relative to permeable spheres. *J. Chemical Engineering Science*. **1973**, *28* (10), 1865−1874.

(18) Johnson, C. P.; Li, X.; Logan, B. E. Settling velocities of fractal aggregates. *J. Environmental science & technology*. **1996**, *30* (6), 1911−1918.

(19) Tsou, G. W.; Wu, R. M.; Yen, P. S.; Lee, D. J.; Peng, X. F. Advective flow and floc permeability. *J. Journal of colloid and interface science*. **2002**, *250* (2), 400−408.

(20) Wu, R. M.; Lee, D. J.; He, P. Estimation of floc permeability and porosity. *J. Chinese Inst. Chem. Eng.* **2003**, *34* (2), 275−280.

(21) Wu, R. M.; Feng, W. H.; Tsai, I. H.; Lee, D. J. An estimate of activated-sludge floc permeability: a novel hydrodynamic approach. *J. Water environment research*. **1998**, *70* (7), 1258−1264.

(22) Tyler, S. W.; Wheatcraft, S. W. Fractal scaling of soil particle-size distributions: Analysis and limitations. *J. Soil Science Society of America Journal*. **1992**, *56* (2), 362−369.

(23) Ahmed, H. A.; Drzymala, J. Two-dimensional fractal linearization of distribution curves. *J. Physicochem. Problems Miner. Proc.* **2005**, *39*, 129−139.

(24) Wang, J.; Fu, X. H.; Zhao, J.; Yang, L. Effect of ultra-fine grinding on coal surface properties and ultra-clean coal separation. *Journal of China Coal Society* **2016**, DOI: 10.13225/j.cnki.jccs.2015.1389.

(25) Carpinteri, A.; Lacidogna, G.; Niccolini, G. Fractal analysis of damage detected in concrete structural elements under loading. *J. Chaos, Solitons & Fractals.* **2009**, *42* (4), 2047−2056.
(26) Zhang, J. J.; Li, Y. T. Fractal features of soil particle size distributions and its effect on soil erosion of Loess Plateau. *J. Transactions of the Chinese Society for Agricultural Machinery* **2015**, *46* (4), 176−182.
(27) Movahedi, H.; Jamshidi, S. Experimental and CFD simulation of slurry flow in the annular flow path using two-fluid model. *J. Journal of Petroleum Science and Engineering.* **2021**, *198*, 108224.
(28) Qi, Y. Study on the drag model of nanoparticle agglomeration based on fractal dimension. MS thesis, Harbin Institute of Technology, 2018. DOI: 10.7666/d.D01587792.
(29) Ramkrishna, D. On aggregating populations. *J. Industrial & engineering chemistry research.* **2004**, *43* (2), 441−448.
(30) Ramkrishna, D.; Singh, M. R. Population balance modeling: current status and future prospects. *J. Annual review of chemical and biomolecular engineering.* **2014**, *5*, 123−146.
(31) Somasundaran, P.; Runkana, V. Modeling flocculation of colloidal mineral suspensions using population balances. *J. International Journal of Mineral Processing.* **2003**, *72* (1−4), 33−55.
(32) Zheng, J. X.; Li, Y. K.; Sun, X. N.; Zhou, H. C. Analysis of collision frequency of non spherical particles in turbulent agglomeration process. *Journal of Chemical Engineering* **2019**, *70*, 228−236.
(33) Song, G.; Li, Y.; Wang, W.; Jiang, K.; Shi, Z.; Yao, S. Hydrate agglomeration modeling and pipeline hydrate slurry flow behavior simulation. *J. Chinese Journal of Chemical Engineering.* **2019**, *27* (1), 32−43.
(34) Ghadiri, M. Particle impact breaking. *J. Handbook of Powder Technology.* **2006**, 205−212.
(35) Carpinteri, A.; Pugno, N. A fractal comminution approach to evaluate the drilling energy dissipation. *J. International journal for numerical and analytical methods in geomechanics.* **2002**, *26* (5), 499−513.
(36) Freitas, C. J. The issue of numerical uncertainty. *J. Applied Mathematical Modelling.* **2002**, *26* (2), 237−248.
(37) Manna, P.; Dharavath, M.; Sinha, P. K.; Chakraborty, D. Optimization of a flight-worthy scramjet combustor through CFD. *J. Aerospace science and technology.* **2013**, *27* (1), 138−146.
(38) Liu, H. L.; Liu, M. M.; Bai, Y.; Du, H.; Dong, L. Grid convergence based on GCI for centrifugal pump. *J. J. Jiangsu Univ. Nat. Sci. Ed.* **2014**, *35*, 279−283.
(39) Gidaspow, D. *Multiphase flow and fluidization: continuum and kinetic theory descriptions*; Academic Press, 1994; pp 337−354.
(40) Guo, Y. Q.; Guo, L. Calculation method of dust laden air flow density. *J. Guangdong Electric Power* **2006**, *19* (10), 3.

https://doi.org/10.1021/acsomega.2c01825
ACS Omega 2022, 7, 21750−21762